J MATER SCI **41** (2006) 2597–2600

Application of energy-filtering TEM to the nanocrystallization process in amorphous $Fe_{84}Nb_7B_9$ alloy

AKIHIKO HIRATA*, YOSHIHIKO HIROTSU
The Institute of Scientific and Industrial Research, Osaka University, Ibaraki, Osaka, 567-0047 Japan

Published online: 17 April 2006

The nanocrystallization process in amorphous $Fe_{84}Nb_7B_9$ alloy was studied by means of energy-filtering transmission electron microscopy. Energy-filtered diffraction intensity provided quantitative structural analysis for the as-quenched state with the help of reverse Monte Carlo simulation. Using the Fe L-edge it was found from chemical mapping that chemical segregation of Fe with Fe-rich and Fe-poor regions starts to occur at the later stage of nanocrystallization.

1. Introduction

Energy-filtering transmission electron microscopy (EFTEM) now becomes one of the effective techniques for characterizing nanometer-scale microstructures of various materials [1]. The EFTEM technique makes it possible to obtain images or diffraction patterns using the desired energy range of the electron energy-loss spectrum (EELS). Two effective applications are widely utilized: one is elemental mapping and the other, qualitative diffraction intensity analysis. The former technique is performed by taking images using energy-loss electrons with the core-loss energy range of any elements. The latter is, on the other hand, is achieved by taking electron diffraction patterns using only the zero-loss electrons to eliminate inelastically scattered electrons. It is important to note that these two techniques bring chemical and structural information of local regions in the materials at the same time when they are combined.

In amorphous Fe-M-B (M = Nb, Zr, Hf) alloys, it is well known that bcc-Fe nanocrystals as small as 10–20 nm are formed with high density on annealing and the structure gives good soft magnetic properties [2, 3]. The mechanism of the nanocrystallization with an extremely high-density nucleation rate is still unsolved [4]. Since the EFTEM can provide both structural and chemical information as mentioned above, it becomes an important technique for understanding the nanocrystallization mechanism in amorphous alloy systems. In this study, we performed electron diffraction intensity analysis and elemental mapping using EFTEM for as-quenched and annealed specimens of $Fe_{84}Nb_7B_9$ alloy.

2. Experimental procedure

2.1. Specimen and investigation

The amorphous $Fe_{84}Nb_7B_9$ alloy was made by the single-roll rapid quenching technique. The size of the ribbon was about 20 mm in width and 20 μm in thickness. Specimens for TEM observation were prepared by using both electropolishing and ion-milling techniques. High-resolution electron micrographs were obtained using a 300 kV TEM (JEM-3000F). Selected-area electron diffraction patterns (SAED) and energy-filtering images (EFI) were taken by a 200 kV TEM (LEO-922D) equipped with an in-column-type energy filter. Elemental mapping was derived from the three-window method [1] and an energy window width of 20 eV was chosen. The electron diffraction structure analysis was performed in the following way.

2.2. Electron diffraction structure analysis and reverse Monte-Carlo simulation

To eliminate an inelastic part of the intensity, SAED patterns were taken by choosing zero-loss electrons with an energy window width of 20 eV. An estimation of the

*Author to whom all correspondence should be addressed.
0022-2461
DOI: 10.1007/s10853-006-7807-x

sample thickness was also performed by using EELS spectrum analysis. The camera length was corrected by taking a diffraction pattern from a film with fine gold particles. The intensity of the diffraction patterns were recorded on the imaging plates (IP) and read using an IP reader (DITABIS micron). From the recorded diffraction intensity, reduced interference functions can be obtained [5] as

$$\mathrm{Qi(Q)} = \frac{[\mathrm{I_{obs}(Q)} - \mathrm{BG(Q)}]\,\mathrm{Q}\langle \mathrm{f}^2\rangle}{\mathrm{BG(Q)}\langle \mathrm{f}\rangle^2} \tag{1}$$

where $\mathrm{I_{obs}(Q)}$ is the observed intensity and Q the scattering vector. BG(Q) denotes the background intensity, which smoothly links the middle points between the intensity maxima and minima of the halo-intensity profile. The Qi(Q) can be transformed to the reduced distribution function as

$$G(r) = \frac{2}{\pi}\int_0^\infty \mathrm{Qi(Q)}\sin(\mathrm{Qr})\mathrm{dQ} = 4\pi r\,[\rho(r) - \rho_0] \tag{2}$$

where $\rho(r)$ is the atomic density, and ρ_0 the average atomic density which can be obtained from the specimen density. The partial distribution function (PDF) $g(r)$ $(= \rho(r)/\rho_0)$ can be derived by $G(r)$.

In order to construct a structural model which explains the obtained interference function, we performed a reverse Monte-Carlo (RMC) simulation [6, 7]. The simulation was made using the RMCA program [8]. In starting the simulation, we prepared an initial structure with a dense-random packing (DRP) 5000 Fe, Nb, and B atoms followed by a static structural relaxation using Lennard-Jones atomic potentials. Atomic density and composition of the initial structure followed the practical ones. The atomic configuration was improved by changing atom positions so as to decrease the mean square deviation χ^2 between $i_{\mathrm{exp}}(\mathrm{Q})$ and $i_{\mathrm{sim}}(\mathrm{Q})$ defined as

$$\chi^2 = \sum \frac{(i_{\mathrm{exp}}(\mathrm{Q}) - x i_{\mathrm{sim}}(\mathrm{Q}))^2}{\sigma(\mathrm{Q})^2} \tag{3}$$

where $i_{\mathrm{exp}}(\mathrm{Q})$ and $i_{\mathrm{sim}}(\mathrm{Q})$ are the interference functions obtained from the experiment and simulation, respectively. The value $\sigma(\mathrm{Q})$ is a parameter related to the experimental error. After obtaining a final structural model, we performed a Voronoi polyhedral analysis to understand a feature of local atomic environments.

3. Experimental results

In Fig. 1a, the experimental interference function (i(Q)) obtained from the as-quenched specimen is compared with that from the RMC simulated result. In the inset, the filtered SAED pattern is shown. As seen in the figure,

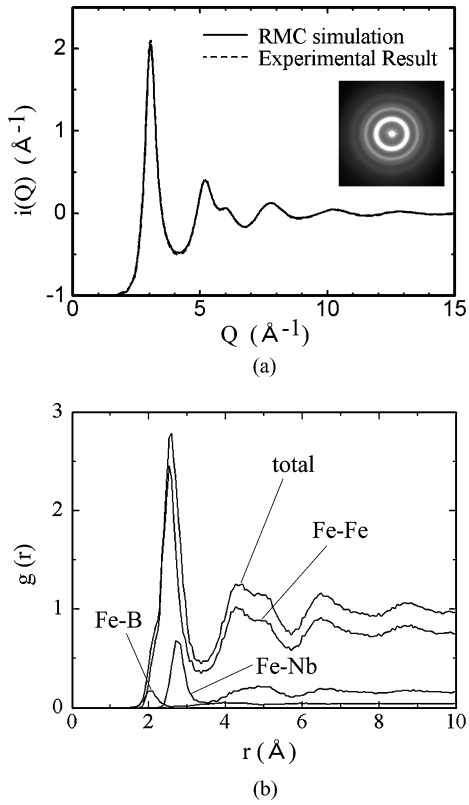

Figure 1 (a) Experimental and RMC simulated interference functions of as-quenched state. (b) Partial pair distribution functions derived from the final RMC model.

the RMC fitting is very good, that is, the final structural model well reproduces the experimental result. Total and partial atomic pair distribution functions (PDF) obtained from the RMC simulation are depicted in Fig. 1b. The peak-top positions of the first peaks for the Fe-Fe, Fe-Nb, and Fe-B partial PDFs are at 0.25, 0.27, and 0.21 nm, respectively. These atomic distances are in good agreement with those obtained by X-ray diffraction [9].

In order to examine the local atomic arrangements in the $Fe_{84}Nb_7B_9$ amorphous alloy, the Voronoi polyhedral analysis was performed for the final RMC structural model. Fig. 2 represents numbers of Voronoi polyhedral structures with central Fe and Nb atoms. In the figure for the central Fe atom, the polyhedra with the index "0 3 6 4 0 0" corresponding to the deformed bcc cluster are frequently observed. Icosahedral-like clusters with indices of "0 2 8 2 0 0" and "0 1 10 2 0 0 0" are also found with high frequency. On the other hand, the polyhedra with central Nb atom are frequently found to have large coordination numbers of 15–16. Hence, the atomic structures in the as-quenched state are found to be composed of bcc or icosahedral-like clusters with central Fe atom and 15–16 coordinated clusters with central Nb atom rather predominantly.

Fig. 3 shows three sets of zero-loss and Fe L-edge core-loss images obtained from specimens annealed up

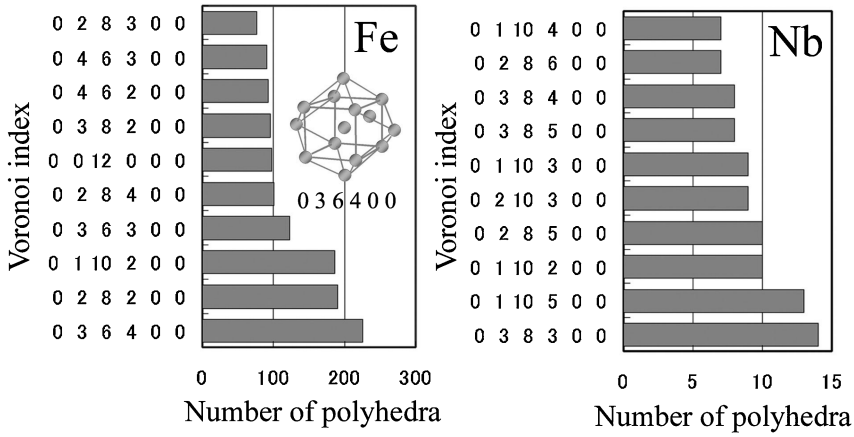

Figure 2 Numbers of Voronoi polyhedra around (a) Fe and (b) Nb atoms obtained from the RMC model for the as-quenched state.

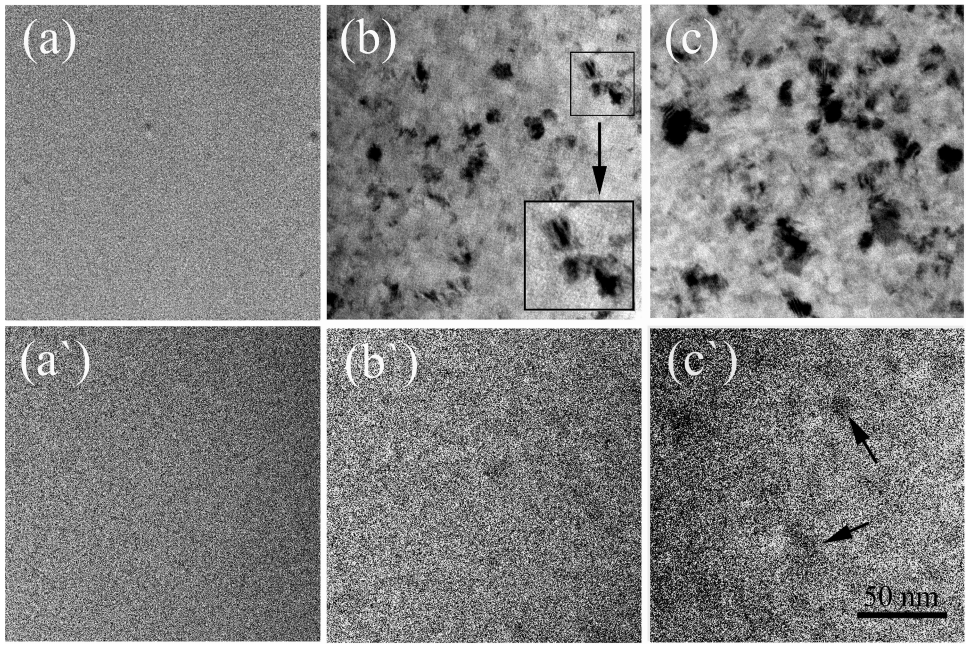

Figure 3 Zero-loss and Fe L-edge images taken from (a)(a′) 773 K, (b)(b′) 843 K, and (c)(c′) 943 K annealed specimens.

to (a)(a′) 773 K, (b)(b′) 843 K, and (c)(c′) 943 K. In the stage annealed up to 773 K, although nanocrystals are found very locally (dark dots) in (a), the Fe mapping in (a′) basically shows homogeneous contrast in the whole region. On the other hand, the annealing up to 843 K led to form a nanocrystalline microstructure where highly dense α-Fe nanocrystals are embedded in the amorphous matrix as shown in an inset of (b). The Fe mapping in (b′) shows an inhomogeneous contrast, that is, the compositional fluctuation due to the α-Fe nanocrystallization can be detected within the limit of resolution of the mapping. In the stage of (c), the compositional fluctuation can be found clearly as indicated by arrows in (c′). An average distance of the compositional fluctuation is directly corresponding to the grain sizes of the nanocrystals.

The high-resolution image obtained from the sample annealed up to 943 K is shown in Fig. 4. In the center of the image, we can see a crystal grain with a size of about 10 nm and lattice fringes with a large interplaner spacing of 0.63 nm in the grain. A FFT pattern taken from the grain is shown in the inset. This pattern is obviously different from that of the bcc-Fe structure. The FFT pattern was found to correspond to the [113] diffraction pattern of the α-Mn type structure, which was already found in the $Fe_{80}Nb_{10}B_{10}$ system [10]. It can be concluded that the compositional fluctuation causes the α-Mn type structure to appear in the Fe-poor region in this system.

4. Discussion

For the nanocrystallization mechanism, the compositional fluctuation prior to the crystal nucleation has been considered as one possible explanation in the Zr-based metallic glass [11]. Based on this model, the amorphous structure has to be chemically decomposed with

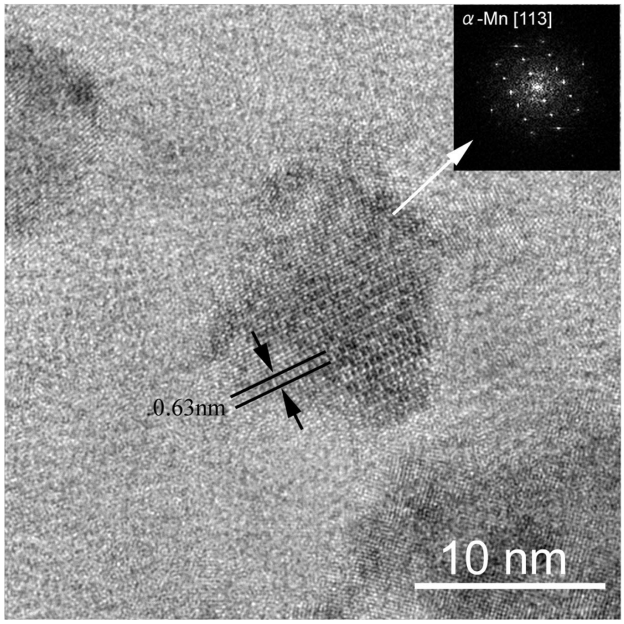

Figure 4 A HREM image of nanocrystal with the α-Mn type structure obtained from annealed specimen up to 943 K. A FFT pattern is also shown in the inset.

a compositional wavelength as large as the distance between the nanocrystals appearing at the later stage. In the present case, however, such compositional fluctuation cannot be detected in the stage at 773 K before the clear nanocrystallization. In addition, the Voronoi analysis indicated that the as-quenched state includes many polyhedral clusters with the bcc-Fe structure, which is just the same structure as that of the nanocrystals. As is well known in the case of Fe-based amorphous alloys like Finemet [12], clusters of insoluble Cu atoms become heterogeneous nucleation sites. But, in the present alloy, there are no insoluble atomic elements. It is reasonable to consider that the inherent bcc-like atomic clusters in the amorphous state partially transform to the nanocrystals with extremely high number density.

In the stage at 943 K, the α-Mn structure was found to appear in consequence of the development of the compositional segregation. It is well known that the α-Mn structure is composed of the coordination polyhedra with 12, 13, and 16 coordination numbers [13]. Note that 12-coordination polyhedron is identical to the icosahedron. From the Voronoi analysis, in the as-quenched state, many icosahedral-like and 15–16 coordinated polyhedra were found just like the coordination polyhedra in the α-Mn structure. Also in the annealing state, the amorphous matrix is expected to include such polyhedra predominantly. Because the polyhedra have dense-packing structures and strong chemical bondings [14], these natures are considered to contribute to the formation of the very fine nanocrystals by confining the atomic diffusion of Fe atoms to prohibit the coarsening α-Fe nanoparticles.

Acknowledgment

This study was partly supported by Special Coordination Funds for Promoting Science and Technology on "Nanohetero Metallic Materials" from the Science and Technology Agency, and partly supported by the Grant in Aid of Ministry of Education, Sports, Culture, Science and Technology, Priority Area on "Materials Science of Bulk Metallic Glasses". Discussions with Profs. E. Matsubara and A. Makino are greatly acknowledged. We thank to Prof. A. Makino for supplying the samples. One of us (A. H.) also acknowledges Dr. Ohkubo and Dr. Naito for developing computer programs, and Dr. Hanada and Mr. Koreeda for their technical help.

References

1. R. F. EGERTON, Electron Energy Loss Spectroscopy in the Electron Microscope, 2nd edition (Plenum Press, New York, 1996).
2. A. MAKINO, A. INOUE and T. MASUMOTO, *Mater. Trans. JIM*, **36** (1995) 924.
3. A. MAKINO, T. HATANAI, A. INOUE and T. MASUMOTO, *Mater. Sci. Eng.* **A226** (1997) 594.
4. H. ASSADI and J. SCHROERS, *Acta Mater.* **50** (2002) 89.
5. S. R. ELLIOTT, "Physics of Amorphous Materials," Section 3 (Longman Science and Technology, Essex, 1990).
6. R. L. MCGREEVY and L. PUSZTAI, *Mol. Simul.* **1** (1988) 359.
7. R. L. MCGREEVY, *J. Phys. Condens. Matter* **13**, (2001) R877.
8. available at http://www.studsvik.uu.se./
9. E. MATSUBARA, S. TANAKA, A. MAKINO and TE-HSUAN CHIANG, *Mater. Trans.* **45** (2004) 1199.
10. M. IMAFUKU, S. SATO, H. KOSHIBA, E. MATSUBARA and A. INOUE, *Scr. Mater.* **44** (2001) 2369 .
11. S. SCHNEIDER, P. THIYAGARAJAN and W. L. JOHNSON, *Appl. Phys. Lett.* **68** (1996) 493 .
12. K. HONO, K. HIRAGA, Q. WANG, A. INOUE and T. SAKURAI, *Acta Metall. Mater.* **40** (1992) 2137 .
13. J. S. KASPER, *Acta Met.* **2** (1954) 456.
14. D. HOBBS, J. HAFNER and D. SPISAK, *Phys. Rev.* **B68** (2003) 014407.